

Electronic Supplementary Information (ESI)

1. Chemicals

Poly(ethylene oxide)-*b*-poly(methyl methacrylate) (PEO₍₁₀₅₀₀₎-*b*-PMMA₍₁₈₀₀₀₎) was obtained from Polymer Source. Tetrahydrofuran (THF) (ACS reagent, $\geq 99.0\%$, contains 250 ppm of inhibitor), sodium hexachlororhodate (III) (Na₃RhCl₆), nickel (II) chloride (NiCl₂) (anhydrous, 99.99%), potassium hydroxide (KOH) solution (45 wt% in H₂O), hydrochloric acid (HCl) (ACS reagent, 37%), and phosphotungstic acid hydrate (reagent grade) were purchased from Sigma-Aldrich. Further purification was not conducted before using all the chemicals.

2. Synthesis of mesoporous Rh_xNi_{100-x} films

Mesoporous Rh_xNi_{100-x} films were electrochemically deposited with the assist of self-assembled micelle as a soft template (**Scheme 1**). First of all, 5 mg of PEO₍₁₀₅₀₀₎-*b*-PMMA₍₁₈₀₀₀₎ was dissolved as unimer in THF by 10-min sonication. After the solution turned transparent, the controlled amount of Na₃RhCl_{6(aq)} and NiCl_{2(aq)} were added to get different-compositions films, and the total volume of these electrolytes was finally increased to 5 mL with distilled water and HCl_(aq) which is for adjusting the pH. It is notable that the continuous addition of aqueous solutions induces the micellization of PEO-*b*-PMMA since the hydrophobic PMMA unit cannot be dissolved in water and is forced to be wrapped inside the hydrophilic PEO unit. Metal precursors tend to form an aqua complex in this water-rich solution; therefore, they can interact with the PEO unit (*i.e.*, the shell of micelles) by hydrogen bonding and decorate micelles. Once the solutions were prepared, electrochemical depositions were conducted with the conventional three-electrodes system composed of Pt wire counter electrode, Ag/AgCl (3 M NaCl) reference electrode, and gold (Au)-coated (200-nm thickness) silicon (Si) substrate as a working electrode. The deposition area was fixed to 0.18 cm² for all samples. All electrochemical measurements were performed with CHI 760E electrochemical analyzer (CHI Instrument, Inc.). The optimal deposition potentials and times were carefully chosen for each sample, as discussed later, and applying negative potentials triggered the reduction reaction of metals on Au/Si working electrode around the micelle templates. By the successive electrochemical deposition, the film thickness reached ~160 nm. The as-prepared films were finally taken out of the reaction bath and immersed in 50 °C chloroform to remove micelles. Then,

they were rinsed with distilled water and dried with nitrogen gas (N₂) flow. The summary of compositions of solutions as well as deposition conditions is listed in **Table S1**.

3. Characterizations

The field emission scanning electron microscope (FE-SEM, JEOL JSM-7100F) was utilized to observe morphologies of the as-prepared mesoporous Rh_xNi_{100-x} films. The thickness and final RhNi composition were also measured with this instrument by cross-sectional mode and X-ray energy dispersive spectroscopy (EDS), respectively. 15 kV accelerating voltage was applied in checking morphologies, while 30 kV was used in EDS analyses. For further investigation on the internal structure as well as element mapping, a transmission electron microscope (TEM, Hitachi HF5000) was adopted with an accelerating voltage of 200 kV. The micelles structure was also checked by a similar TEM machine, Hitachi HT7700. As another experiment to study micelles in solutions, small-angle neutron scattering (SANS) measurements were performed with the Bilby instrument¹ in velocity selector mode with a neutron wavelength of 6 Å and detector distances of 6.8 m (rear detector), 3.5 m (horizontal curtains) and 2.5 m (vertical curtains). Data were reduced using Mantid² and standard procedures.

In order to study the crystal structure of films, X-ray diffraction (XRD) measurements were implemented with Rigaku Smart Lab using Cu Kα radiation at the speed of 2 degrees min⁻¹. Since our samples were thin (~ 160 nm), the grazing incidence (GI) mode was useful to avoid diffraction peaks generated by the Au substrate. The chemical states on the surface were analyzed by X-ray photoelectron spectroscopy (XPS, Kratos Axis Ultra XPS) with a monochromatic Al Kα (1486.6 eV) X-ray source. The charge correction was done with the reference of C-C bond at 284.8 eV.

4. Electrochemical measurements (hydrogen evolution reaction (HER))

HER performances were tested by CHI 760E with the typical setup including counter electrode (carbon rod), reference electrode (saturated calomel electrode (SCE)), and the working electrode (our mesoporous Rh_xNi_{100-x} films on Au/Si substrate). The geometrical surface areas of deposited films are 0.18 cm² (0.3 × 0.6 cm) for all samples, and the recorded currents are normalized to this value. 1 M KOH solution was used as an

electrolyte, and it was pre-purged by N₂ for 20 min to remove dissolved oxygen. Before testing HER performances, the as-prepared samples were electrochemically activated by running 100-cycles cyclic voltammetry (CV) from -1.05 V to 0 V (vs. SCE) at the scan rate of 500 mV s⁻¹. (**Step 1**) Another 3-cycles CV were subsequently collected with a slower scan rate (20 mV s⁻¹), and the third CV was extracted for the calculation of the electrochemically active surface area (ECSA). (**Step 2**) In order to get stable data, we firstly ran 100-cycles CV from -1.0 V to -1.3 V (vs. SCE) at the scan rate of 100 mV s⁻¹. (**Step 3**) Then, the polarization curves related to HER were recorded by linear sweep voltammetry (LSV) from -1.0 V to -1.4 V at the scan rate of 2 mV s⁻¹. (**Step 4**) It is notable that the potential sweeps were completed until the current density reached 100 mA cm⁻². Finally, electrochemical impedance spectroscopy (EIS) measurements were implemented to study solution resistance (*R_s*) and charge transfer resistance (*R_{ct}*) with a frequency range of 1 ~ 10000 Hz. These *R_s* values were used for *iR* compensation. Regarding mesoporous Ni₁₀₀ film, different potential ranges (vs. SCE) were applied for each steps; -1.3 V ~ -0.5 V (**Step 1, 2**) (CV for ECSA calculation was collected at the scan rate of 50 mV s⁻¹), -1.0 ~ -1.5 V (**Step 3**), and -1.0 ~ -1.6 V (**Step 4**). This is because the Ni was immediately dissolved (unlike RhNi alloys) in the solution by sweeping the potentials to > -0.5 V, and more negative potentials were needed to reduce the oxidized surface formed in the anodic scan completely. The higher scan rate in **Step 1, 2** was adopted to detect a smaller current than the case of Rh-based films. For further analyses on HER activities, overpotentials were calculated by the following equation;

$$V_{RHE} = V_{SCE} + 0.241 + 0.059 \times pH + |I| \times R_s \quad (1)$$

here, *V_{RHE}* and *V_{SCE}* are the overpotentials versus RHE and the measured potentials versus SCE, respectively. pH in this experiment is 14 (1 M KOH); thus, **equation (1)** can be written as follows;

$$V_{RHE} = V_{SCE} + 1.067 + |I| \times R_s \quad (2)$$

The last term represents *iR* compensation.

Finally, the HER stability of mesoporous Rh₁₀₀, Rh₄₉Ni₅₁, and Ni₁₀₀ films was tested by chronopotentiometry at the current density of 10 mA cm⁻² for 10 hours.

Table S1 Compositions of reaction solutions and deposition conditions for preparing mesoporous films. All solutions contain the same amount of PEO₍₁₀₅₀₀₎-*b*-PMMA₍₁₈₀₀₀₎ (5 mg) and THF (0.5 mL), and pH was adjusted with HCL_(aq). (Total amount of all solutions is 5 mL.)

Samples	Na ₃ RhCl ₆ [mM]	NiCl ₂ [mM]	Rh ³⁺ [mol%]	Ni ²⁺ [mol%]	pH	Potential [V]	Time [s]
Rh ₁₀₀	6.4	0	100	0	3.5	-0.7	300
Rh ₉₃ Ni ₇	6.4	0.8	88.9	11.1	3.5	-0.7	290
Rh ₈₃ Ni ₁₇	6.4	1.6	80	20	3.5	-0.7	280
Rh ₇₆ Ni ₂₄	6.4	3.2	66.7	33.3	3.6	-0.7	270
Rh ₅₈ Ni ₄₂	6.4	6.4	50	50	3.6	-0.7	240
Rh ₄₉ Ni ₅₁	6.4	12.8	33.3	66.7	3.6	-0.7	180
Ni ₁₀₀	0	6.4	0	100	2.4	-1.2	600
Fig. S8a	6.4	1.6	80	20	3.5	-0.7	500
Fig. S8b	4.0	4.0	50	50	3.5	-0.7	500
Fig. S8c	1.6	6.4	20	80	3.5	-0.7	500

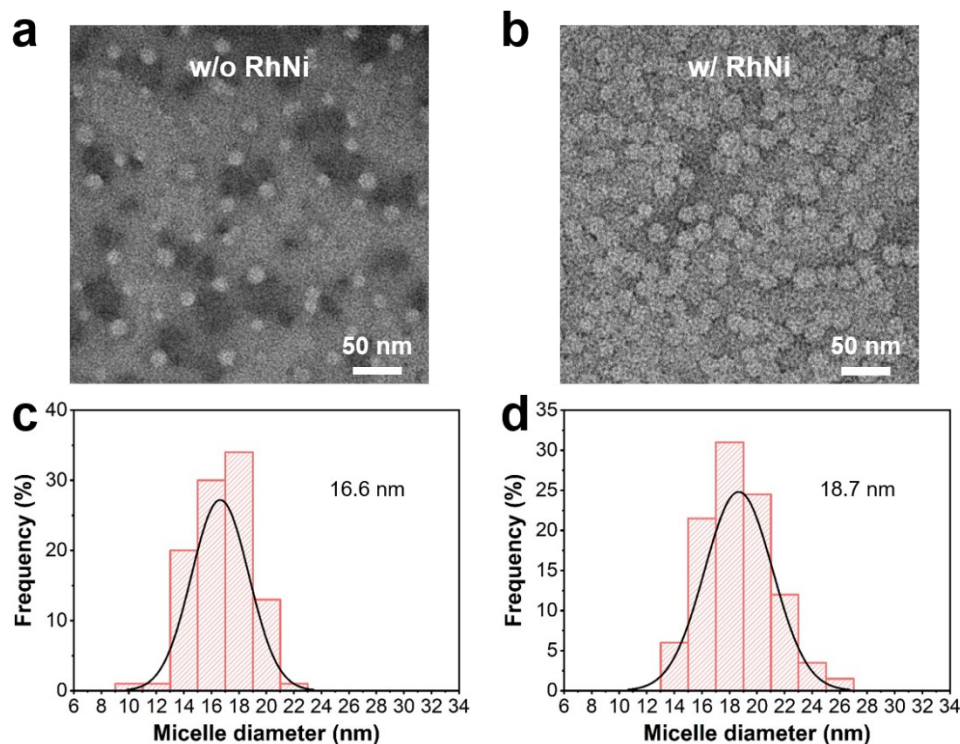


Fig. S1 The TEM images of micelles formed in the solution of (a) $\text{PEO}_{(10500)}\text{-}b\text{-PMMA}_{(18000)}$ + THF + HCl + water, and (b) $\text{PEO}_{(10500)}\text{-}b\text{-PMMA}_{(18000)}$ + THF + Na_3RhCl_6 + NiCl_2 + HCl + water, which is same composition as the solution generating mesoporous $\text{Rh}_{49}\text{Ni}_{51}$ film. (c, d) The histogram of micelle diameter measured over 100 micelles in the corresponding TEM images. (The inset numbers are the average values.)

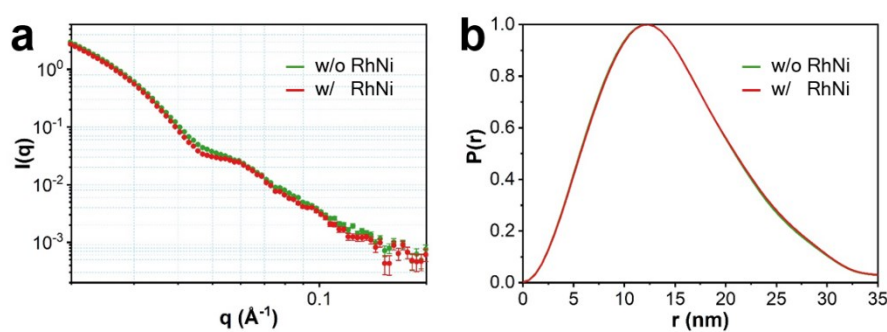


Fig. S2 (a) SANS plots and (b) radial probability distribution functions obtained from the micelle solutions w/ (red) and w/o (green) metal precursors. (The solution compositions are the same as the case of TEM observation shown in **Fig. S1** except that the solvents were replaced with the deuterated equivalent ones)

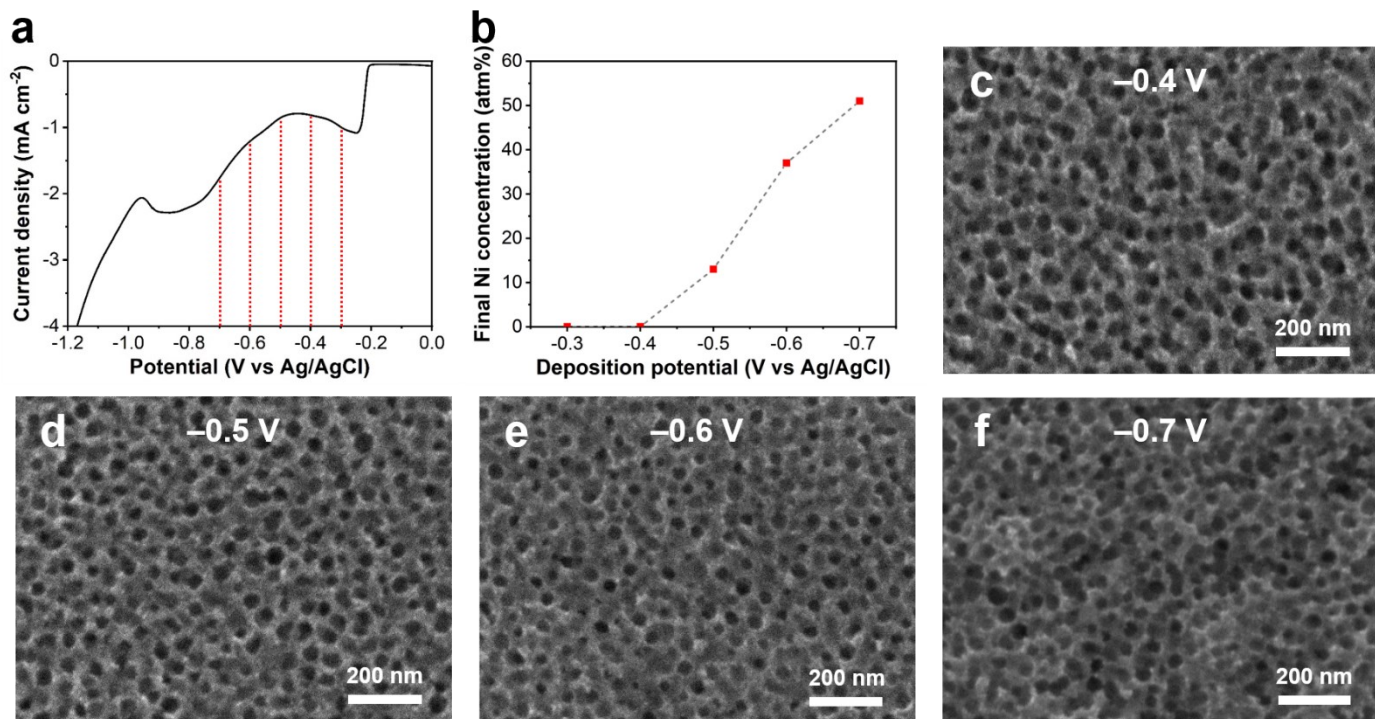


Fig. S3 (a) LSV curve obtained at the scan rate of 5 mV s^{-1} in the deposition solution for mesoporous $\text{Rh}_{49}\text{Ni}_{51}$ film (b) The plots of Ni concentrations confirmed by SEM-EDS in the various samples deposited at -0.3 , -0.4 , -0.5 , -0.6 , -0.7 V for 180 s in the corresponding deposition solution. (c-f) Top-surface SEM images of the samples deposited at each potential.

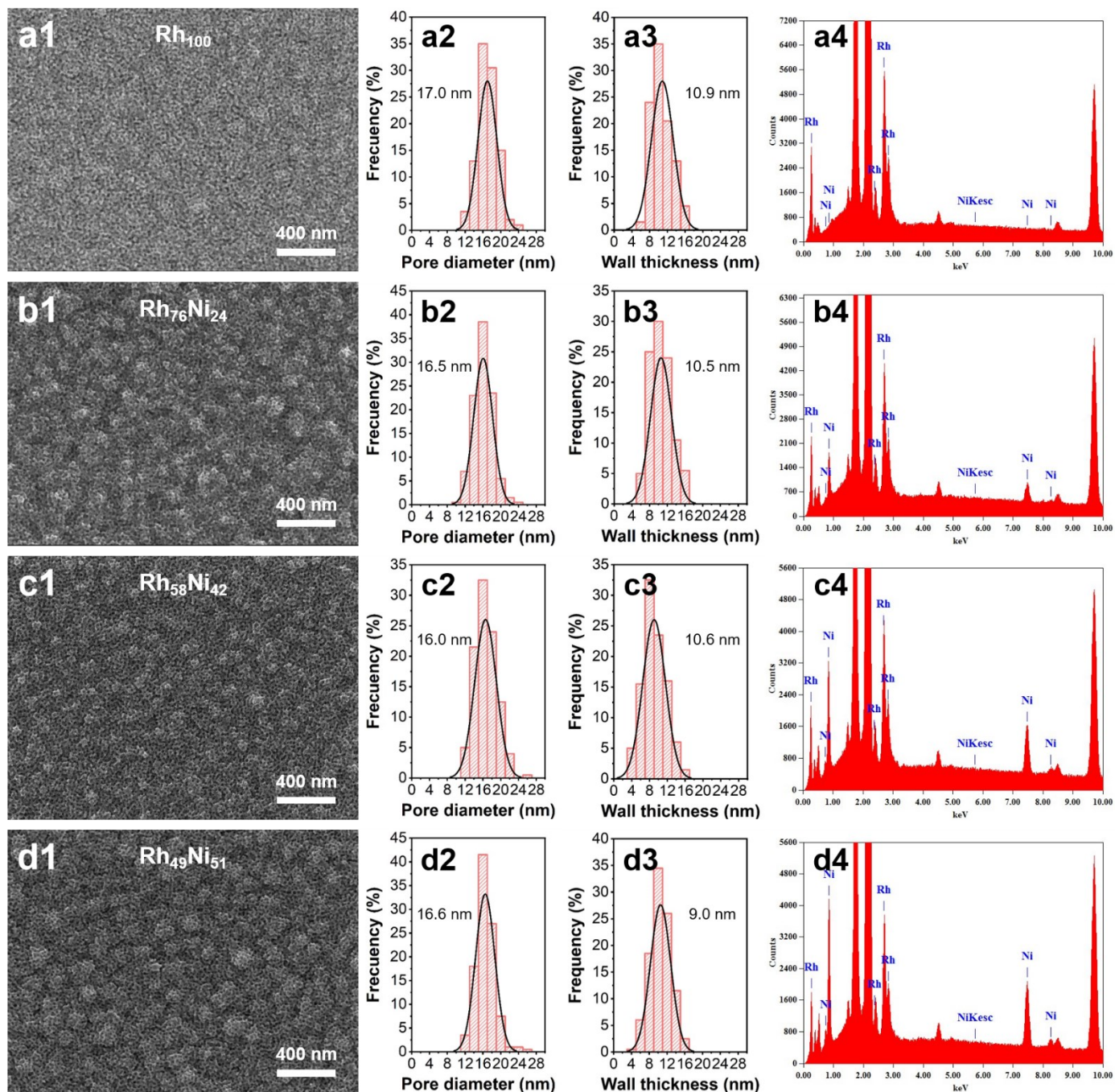


Fig. S4 (a1-d1) Low-magnification top-surface SEM images of mesoporous Rh₁₀₀, Rh₇₆Ni₂₄, Rh₅₈Ni₄₂, Rh₄₉Ni₅₁ films (a2-d2) The histograms of pore diameters and (a3-d3) pore wall thickness measured in the corresponding SEM images. (The inset shows the average values.) (a4-d4) The corresponding SEM-EDS spectra showing the presence of Rh and Ni.

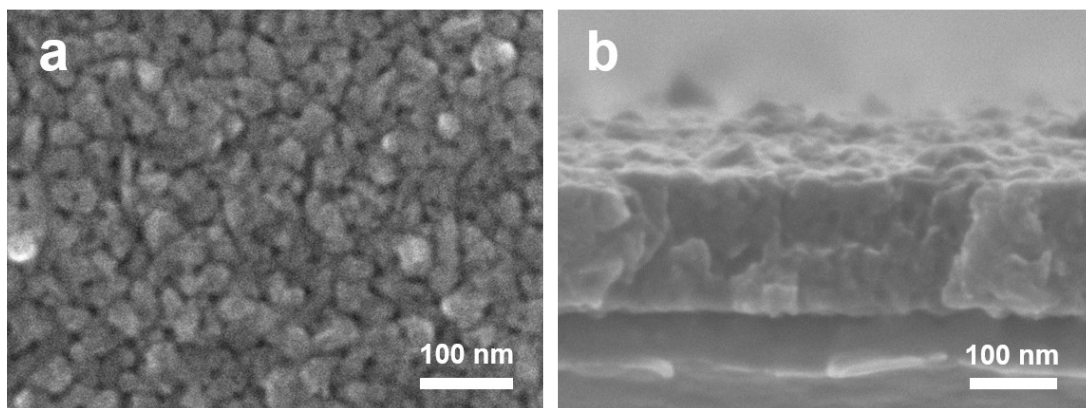


Fig. S5 (a) Top-surface and (b) cross-sectional SEM images of mesoporous Ni₁₀₀ film

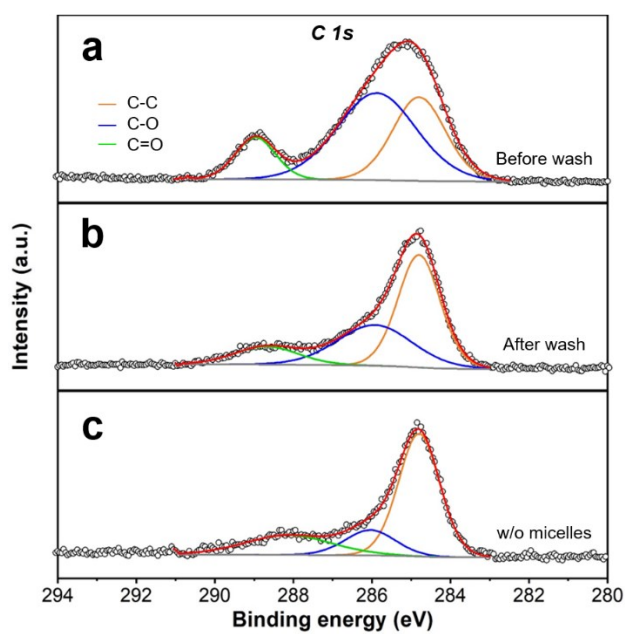


Fig. S6 C 1s XPS spectra of mesoporous Rh₄₉Ni₅₁ film before (a) and after (b) washing the micelles, and the sample prepared in the absence of micelles (c).

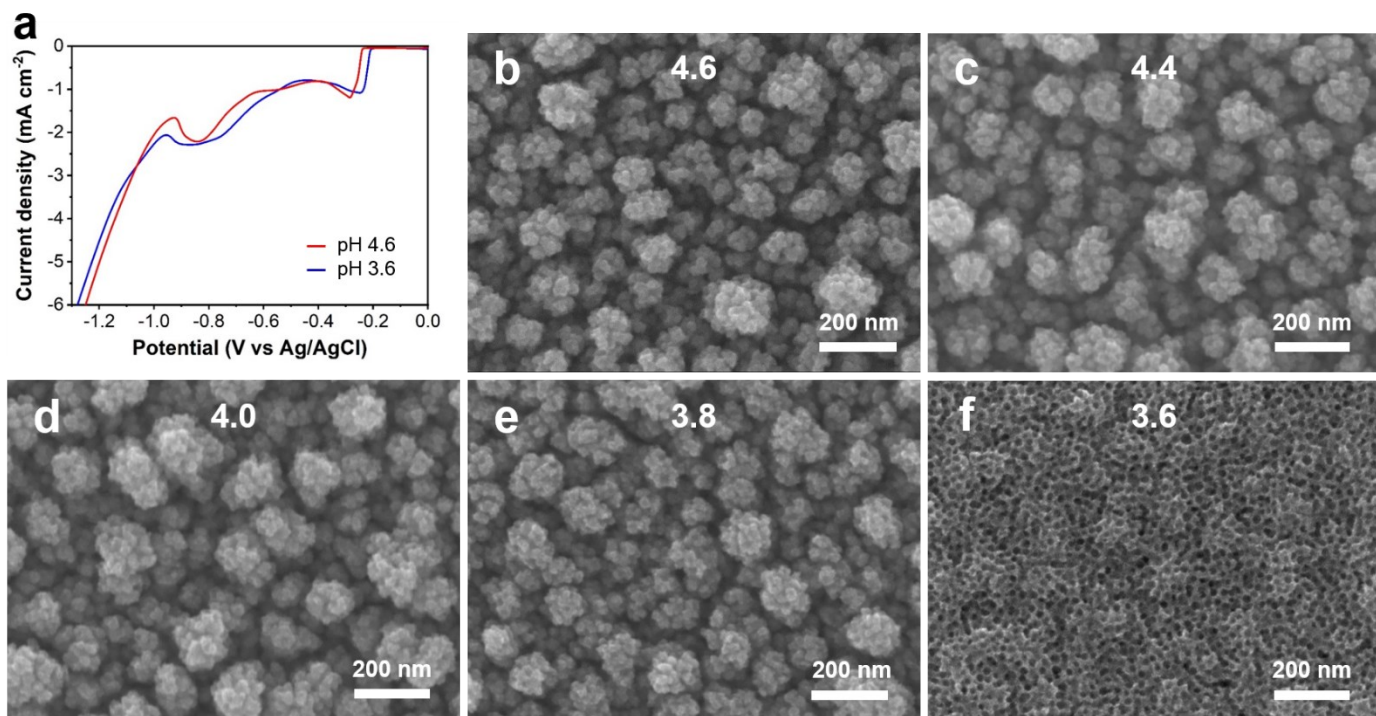


Fig. S7 (a) LSV curves recorded at the scan rate of 5 mV s^{-1} in the deposition solution for mesoporous $\text{Rh}_{49}\text{Ni}_{51}$ film (blue, pH = 3.6) and the same solution but the absence of $\text{HCl}_{(\text{aq})}$ (red, pH = 4.6). (b-f) Top-surface SEM images of the samples deposited in different pH conditions at -0.7 V for 180 s.

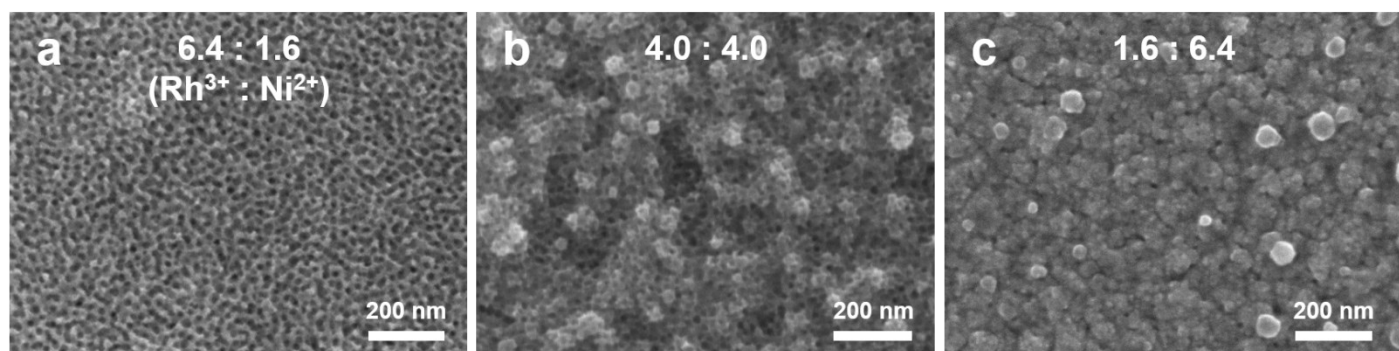


Fig. S8 The experiment to control the final RhNi ratio where the total metal precursor concentration is fixed to 8 mM. (a-c) Top-surface SEM images of the samples prepared from different solutions with the Rh^{3+} concentrations of (a) 6.4, (b) 4.0, and (c) 1.6 mM, where the Ni^{2+} concentrations are 1.6, 4.0, and 6.4, respectively. The final compositions were determined by SEM-EDS to be $\text{Rh}_{90}\text{Ni}_{10}$, $\text{Rh}_{78}\text{Ni}_{22}$, and $\text{Rh}_{49}\text{Ni}_{51}$, respectively. Depositions were conducted at -0.7 V for 500 s, which is set longer than the typical condition since the deposition rate is much slower when Rh^{3+} concentration is low (See **Table S1** for detail information.).

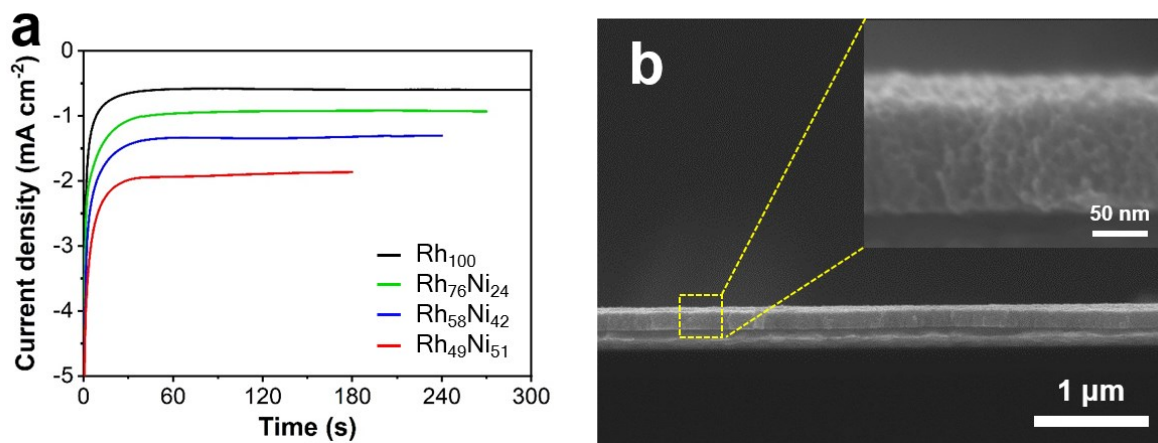


Fig. S9 (a) Amperometric *i-t* curves collected during deposition of mesoporous $\text{Rh}_x\text{Ni}_{100-x}$ films. (b) Cross-sectional SEM image of mesoporous $\text{Rh}_{49}\text{Ni}_{51}$ film with a close look at the yellow area.

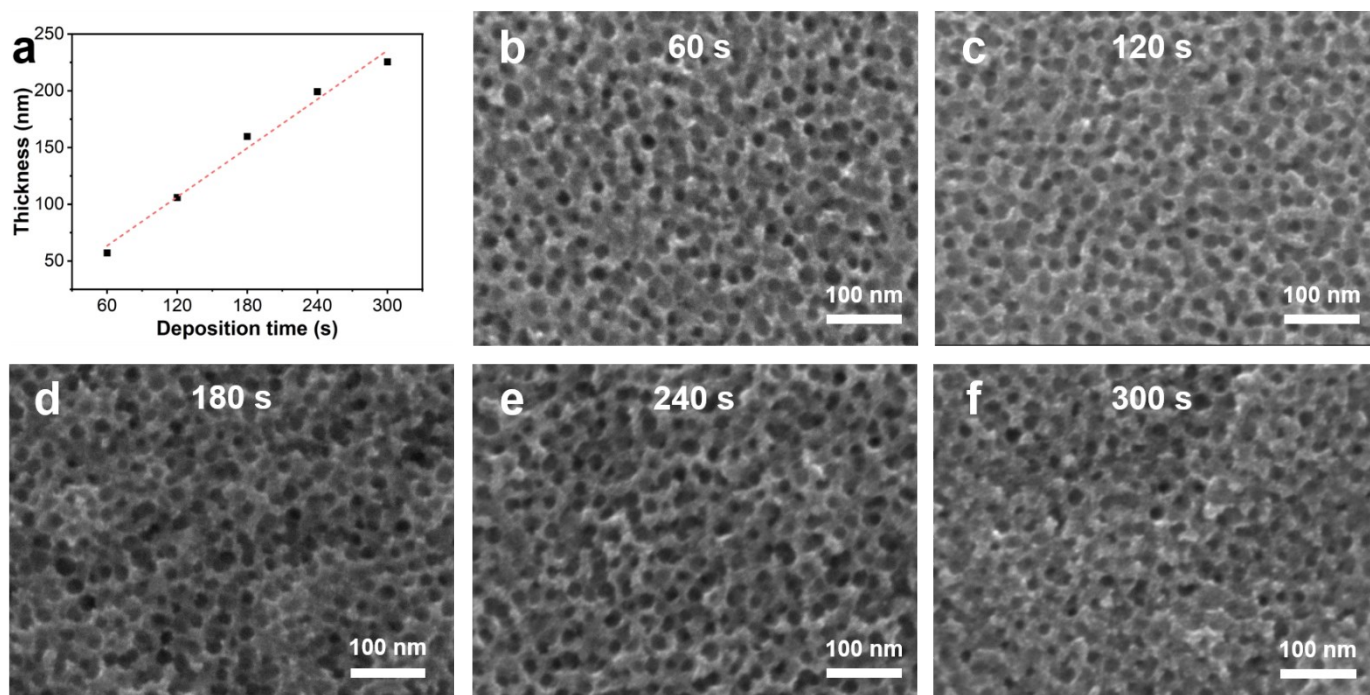


Fig. S10 (a) The plots of film thickness against the deposition times. (The samples were prepared under the same condition for mesoporous $\text{Rh}_{49}\text{Ni}_{51}$ film synthesis while changing the deposition times.) (b-f) Top-surface SEM images of the samples after 60, 120, 180, 240, and 300-s deposition. The final compositions were determined by SEM-EDS to be $\text{Rh}_{63}\text{Ni}_{37}$, $\text{Rh}_{49}\text{Ni}_{51}$, $\text{Rh}_{49}\text{Ni}_{51}$, $\text{Rh}_{47}\text{Ni}_{53}$, and $\text{Rh}_{54}\text{Ni}_{46}$, respectively.

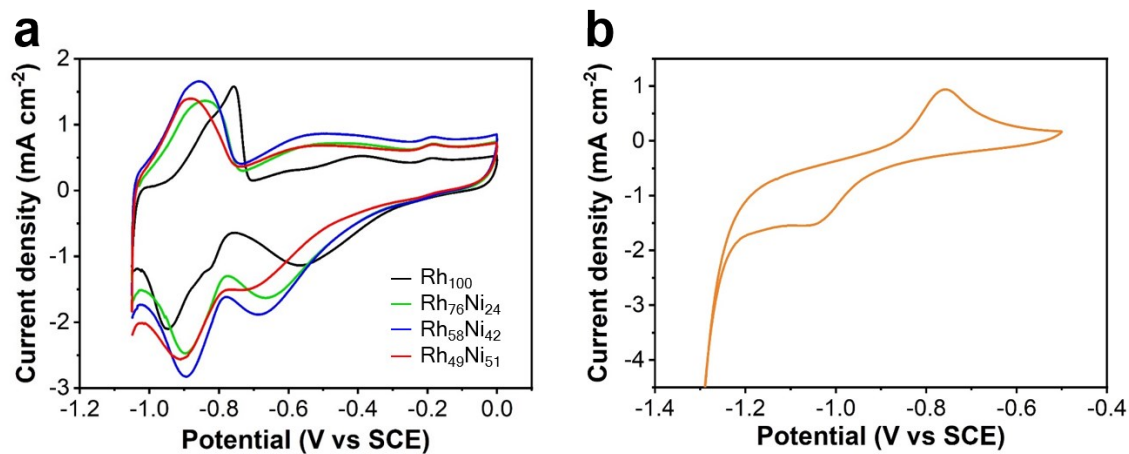


Fig. S11 CVs of the as-prepared mesoporous (a) Rh-based, and (b) Ni₁₀₀ films collected in 1 M KOH solution. (The scan rates are set to 20 mV s⁻¹ except for the case of mesoporous Ni₁₀₀ film (50 mV s⁻¹).

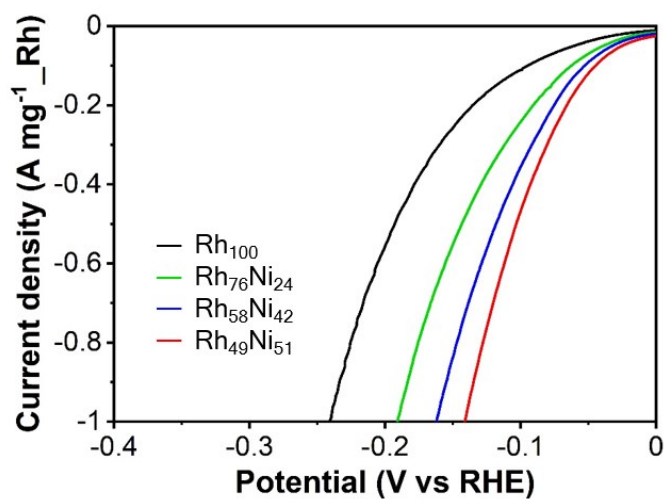


Fig. S12 Rh-mass-normalized HER polarization curves of mesoporous Rh₁₀₀, Rh₇₆Ni₂₄, Rh₅₈Ni₄₂, Rh₄₉Ni₅₁, and Ni₁₀₀ films recorded at the scan rate of 2 mV s⁻¹ in 1 M KOH solution.

Table S2 Comparison of the alkaline-mediated HER activity with Rh- and Ni-based, and other various catalysts. (Rotation rate of 1600 rpm is applied when RDE is used as a working electrode except for ref. 21.)

Catalyst	Loading mass		Electrode	Electrolyte	Scan rate [mV s ⁻¹]	Overpotential [mV] @10 mA cm ⁻²	Tafel slope [mV dec ⁻¹]	Reference
	[μg]	[mg cm ⁻²]						
Mesoporous Rh ₄₉ Ni ₅₁ film	18	0.1	Au/Si substrate	1 M KOH	2	59	67	This work
Rh NSs/C	3	0.015	GCE	0.1 M KOH 1 M KOH	10	37 43	74.7 107.2	3
RhOOH NSs/C-OH-40 (after 40 CVs activation cycles)	2.5 (Rh)	0.0128 (Rh)	GCE	1 M KOH	5	18	19,3	4
RhO ₂ SLNP	14	0.2	GCE	1 M KOH	5	8	12	5
Rh-Rh ₂ O ₃ NPs/C	2	0.028	RDE	0.5 M KOH	10	63	70	6
Rh ₂ P NPs/C (Rh ₂ P: 14.7 wt%)	30	0.15	RDE	1 M KOH	5	30	50	7
Rh/NiFeRh-LDH (Ni/Fe/Rh = 67.5:31.2:1.3 atm%)	7200	1.2	Ni foam	1 M KOH	5	58	81.3	8
Rh SAC-CuO NAs/CF (Rh: 6.8 wt%)	331	0.331	CF	1 M KOH	2	44	---	9
Pt ₅ /HMCS (Pt: 5.08 wt%)	125	0.5	CFP	1 M KOH	1	46.2	48.1	10
Pt ₃ Ni ₃ NWs/C-air (Pt:Ni atomic ratio = 48.9:51.1)	3 (Pt)	0.0153 (Pt)	RDE	1 M KOH	10	40	---	11
PtNi NDs (Pt: 69.58 wt%)	12	0.17	RDE	0.5 M KOH	5	45	52	12
Ru@C ₂ N (Ru: 28.7 wt%)	20	0.285	RDE	1 M KOH	5	17	38	13
Co-substituted Ru NSs	30	0.153	RDE	1 M KOH	5	13	29	14

RuCu NSs/C-250°C (Rh/Cu atomic ratio = 5.5)	---	---	GCE	1 M KOH	5	20	15.3	15
RuP ₂ @NPC (Ru: 22.3 wt%)	70.7	1	GCE	1 M KOH	5	52	69	16
PdP ₂ @CB (Pd: 6.3 wt%)	20	0.283	GCE	1 M KOH	5	35.4	42.1	17
PdNi/CNFs-1:2 (Pd:Ni precursor ratio = 1:2)	---	---	Al foil	1 M KOH	5	187	93	18
Ni-Ni ₃ C/CC	750	3	CC	1 M KOH	5	98	88.5	19
Ni-C-N NSs	25	0.2	RRDE	1 M KOH	2	30.8	---	20
Ni-WN/CC	---	8.9	CC	1 M KOH	5	47	71	21
NiCoN/C nanocages (NiCoN : 76.9 wt%)	40	0.204	RDE	1 M KOH	5	103	---	22
1T-MoS ₂ /Ni ^{2+σ} O _σ (OH) _{2-σ} (1:1) (mass ratio = 1:1)	400	0.8	CFP	1 M KOH	5	73	75	23
	---	4	Ni foam			43	---	
TiO ₂ NDs/Co NSNTs (TiO ₂ /Co mass ratio: 0.3)	750	0.75	CFs	1 M KOH	5	108	62	24

*NSs: nanosheets, GCE: glassy carbon electrode, NPs: nanoparticles, RDE: (glassy carbon) rotating disk electrode, LDH: layered double hydroxide, SAC: single-atom site catalysts, NAs: nanowire arrays, CF: copper foam, Pt₅: Pt clusters from Pt₅(GS)₁₀, GS: deprotonated glutathione, HMCS: hollow mesoporous carbon spheres, CFP: carbon fiber paper, NWS: nanowires, NDs: nanodendrites, SLNP: strawberry-like nanoparticles, NPC: N, P dual-doped carbon, CB: carbon black, CC: carbon cloth, NSNTs: nanosheet-nanotubes, CFs: carbon fibers

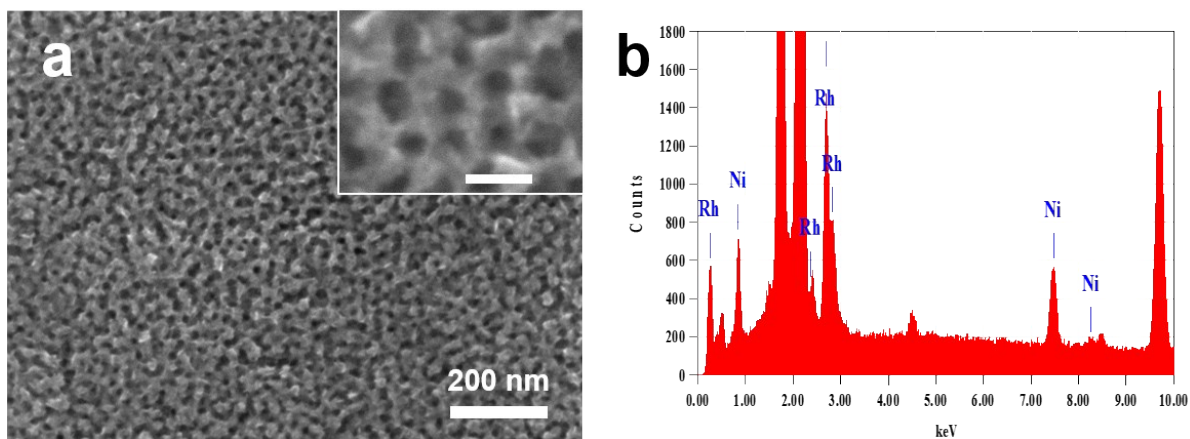


Fig. S13 (a) The top-surface SEM image and (b) SEM-EDS spectrum (the measured Rh : Ni ratio is 52 : 48) of mesoporous $\text{Rh}_{49}\text{Ni}_{51}$ film after 10-h stability test. The insert in (a) is the enlarged SEM image with the 50-nm scale bar.

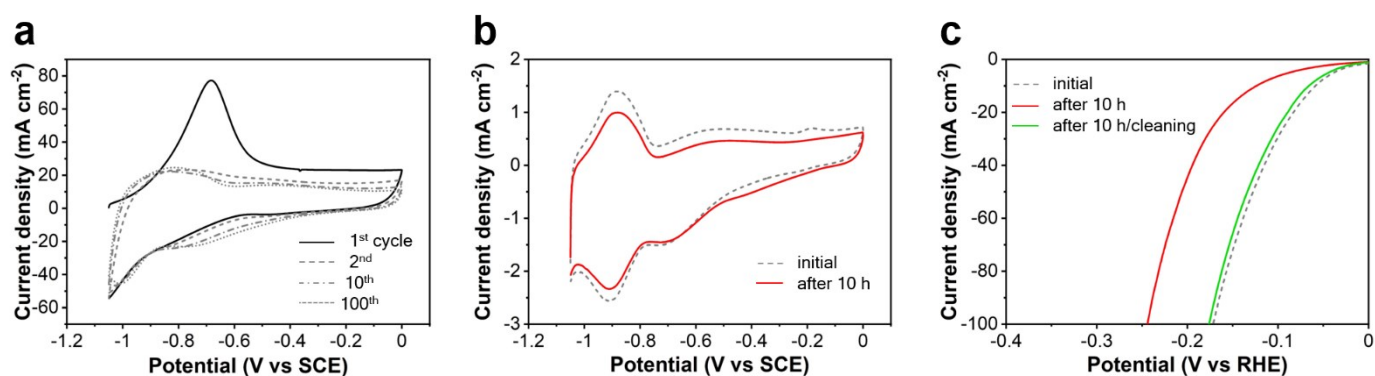


Fig. S14 CVs and HER polarization curves of mesoporous $\text{Rh}_{49}\text{Ni}_{51}$ film in 1 M KOH solution. (a) The selected CVs collected at the scan rate of 500 mV s^{-1} during the electrochemical cleaning process after 10 h stability test. (b) CVs at the slower scan rate of 20 mV s^{-1} before (gray, dash) and after (red, solid) 10-h HER stability test. (c) HER polarization curves before (gray, dash), after 10-h stability test (red, solid), and after additional electrochemical cleaning process (green, solid).

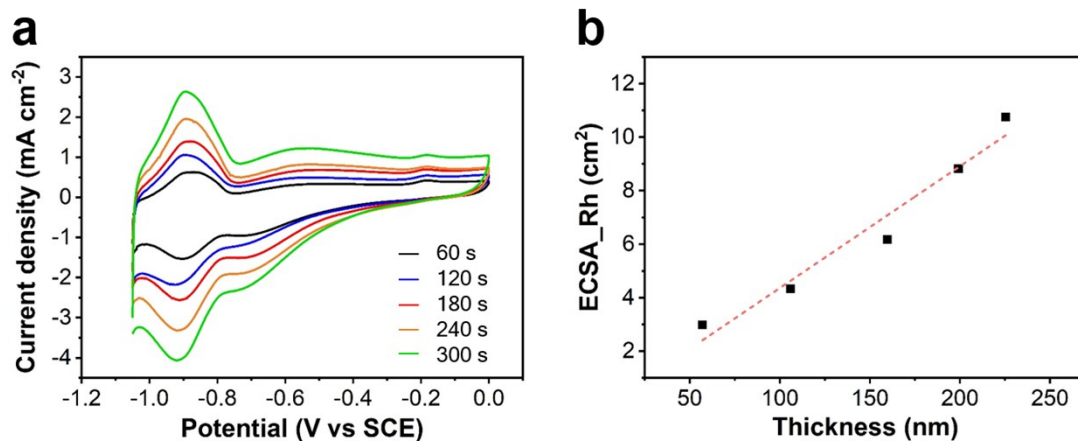


Fig. S15 (a) CVs of mesoporous RhNi films (Rh : Ni \approx 1 : 1) prepared at the same condition as the synthesis of mesoporous Rh₄₉Ni₅₁ film but changing the deposition times from 60 to 300 s.

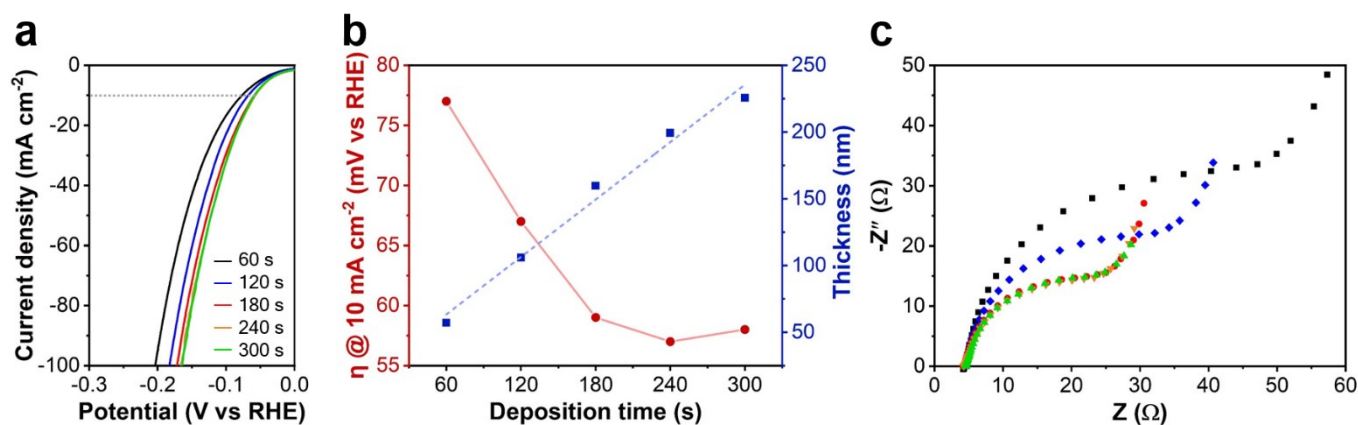


Fig. S16 Alkaline-mediated HER performance of various-thickness (deposition time) mesoporous Rh₄₉Ni₅₁ films in 1 M KOH solution. (The compositions of Rh and Ni are not exactly the same for all samples as described in Fig. S10.) (a) Polarization curves of the samples deposited for 60, 120, 180, 240, and 300 s recorded at the scan rate of 2 mV s⁻¹. (b) The plot of overpotentials at the current density of 10 mA cm⁻², and (c) EIS extracted from the corresponding samples.

Reference

- 1 A. Sokolova, A. E. Whitten, L. De Campo, J. Christoforidis, A. Eltobaji, J. Barnes, F. Darmann, and A. Berry, *J. Appl. Crystallogr.*, 2019, **52**, 1-12.
- 2 O. Arnold, J. C. Bilheux, J. M. Borreguero, A. Buts, S. I. Campbell, L. Chapon, M. Doucet, N. Draper, R. Ferraz Leal, M. A. Gigg, V. E. Lynch, A. Markvardsen, D. J. Mikkelsen, R. L. Mikkelsen, R. Miller, K. Palmén, P. Parker, G. Passos, T. G. Perring, P. F. Peterson, S. Ren, M. A. Reuter, A. T. Savici, J. W. Taylor, R. J. Taylor, R. Tolchenov, W. Zhou and J. Zikovsky, *Nucl. Instrum. Methods. Phys. Res. A*, 2014, **764**, 156-166.
- 3 N. Zhang, Q. Shao, Y. Pi, J. Guo, and X. Huang, *Chem. Mater.*, 2017, **29**, 5009-5015.
- 4 S. Bai, M. Xie, T. Cheng, K. Cao, Y. Xu, and X. Huang, *Nano Energy*, 2020, **78**, 105224.
- 5 Z. Li, Y. Feng, Y.-L. Liang, C.-Q. Cheng, C.-K. Dong, H. Liu, and X.-W. Du, *Adv. Mater.*, 2020, **32**, 1908521.
- 6 M. K. Kundu, R. Mishra, T. Bhowmik, and S. Barman, *J. Mater. Chem. A*, 2018, **6**, 23531-23541.
- 7 F. Yang, Y. Zhao, Y. Du, Y. Chen, G. Cheng, S. Chen, and W. Luo, *Adv. Energy Mater.*, 2018, **8**, 1703489.
- 8 B. Zhang, C. Zhu, Z. Wu, E. Stavitski, Y. H. Lui, T.-H. Kim, H. Liu, L. Huang, X. Luan, L. Zhou, K. Jiang, W. Huang, S. Hu, H. Wang, and J. S. Francisco, *Nano Lett.*, 2020, **20**, 136-144.
- 9 H. Xu, T. Liu, S. Bai, L. Li, Y. Zhu, J. Wang, S. Yang, Y. Li, Q. Shao, and X. Huang, *Nano Lett.*, 2020, **20**, 5482-5489.
- 10 X.-K. Wan, H. B. Wu, B. Y. Guan, D. Luan, and X. W. Lou, *Adv. Mater.*, 2020, **32**, 1901349.
- 11 P. Wang, K. Jiang, G. Wang, J. Yao, and X. Huang, *Angew. Chem. Int. Ed.*, 2016, **55**, 12859-12863.
- 12 X.-Y. Huang, A.-J. Wang, L. Zhang, K.-M. Fang, L.-L. Wu, and J.-J. Feng, *J. Colloid Interface Sci.*, 2018, **531**, 578-584.
- 13 J. Mahmood, F. Li, S.-M. Jung, M. S. Okyay, I. Ahmad, S.-J. Kim, N. Park, H. Y. Jeong, and J.-B. Baek, *Nat. Nanotechnol.*, 2017, **12**, 441-446.
- 14 J. Mao, C.-T. He, J. Pei, W. Chen, D. He, Y. He, Z. Zhuang, C. Chen, Q. Peng, D. Wang, and Y. Li, *Nat. Commun.*, 2018, **9**, 4958.
- 15 Q. Yao, B. Huang, N. Zhang, M. Sun, Q. Shao, and X. Huang, *Angew. Chem. Int. Ed.*, 2019, **58**, 13983-13988.
- 16 Z. Pu, I. S. Amiinu, Z. Kou, W. Li, and S. Mu, *Angew. Chem. Int. Ed.*, 2017, **56**, 11559-11564.
- 17 F. Luo, Q. Zhang, X. Yu, S. Xiao, Y. Ling, H. Hu, L. Guo, Z. Yang, L. Huang, W. Cai, and H. Cheng, *Angew. Chem. Int. Ed.*, 2018, **57**, 14862-14867.
- 18 J. Chen, J. Chen, D. Yu, M. Zhang, H. Zhu, and M. Du, *Electrochim. Acta*, 2017, **246**, 17-26.
- 19 P. Wang, R. Qin, P. Ji, Z. Pu, J. Zhu, C. Lin, Y. Zhao, H. Tang, W. Li, and S. Mu, *Small*, 2020, **16**, 2001642.
- 20 J. Yin, Q. Fan, Y. Li, F. Cheng, P. Zhou, P. Xi, and S. Sun, *J. Am. Chem. Soc.*, 2016, **138**, 14546-14549.
- 21 Z. Xing, D. Wang, Q. Li, A. M. Asiri, and X. Sun, *Electrochim. Acta*, 2016, **210**, 729-733.
- 22 J. Lai, B. Huang, Y. Chao, X. Chen, and S. Guo, *Adv. Mater.*, 2019, **31**, 1805541.
- 23 X. Zhang, and Y. Liang, *Adv. Sci.*, 2018, **5**, 1700644.
- 24 J.-X. Feng, H. Xu, Y.-T. Dong, X.-F. Lu, Y.-X. Tong, and G.-R. Li, *Angew. Chem. Int. Ed.*, 2017, **56**, 2960-2964.